The International Journal of Advanced Manufacturing Technology
https://doi.org/10.1007/s00170-022-08684-5

ORIGINAL ARTICLE

# Numerical modelling and experimental analysis on angular strain induced by bead-on-plate SS316L GMAW using inherent strain and thermomechanical methods

**Siti Nursyahirah Ahmad[1] · Yupiter H. P. Manurung[1] · Keval P. Prajadhiana[1] · Yusuf O. Busari[1] · Muhd Faiz Mat[1] · Norasiah Muhammad[2] · Martin Leitner[3] · Salina Saidin[4]**

Received: 2 September 2021 / Accepted: 4 January 2022
© The Author(s), under exclusive licence to Springer-Verlag London Ltd., part of Springer Nature 2022

**Abstract**
This study presents a basic investigation on angular strain behaviour of substrate using experiment and three different numerical computations based on elastic and elastic–plastic FEM methods. In simulation, a 3D simplified rectangular weld bead geometry was modelled and computed using general purposed numerical software MSC Marc/Mentat. While elastic FEM with well-known inherent strain method-user defined (ISM-UD) and new ISM weld-kinematics (ISM-WK) were applied in which the inherent strain values were empirically estimated with regard to process parameters, physical properties, and effective area on heat affected zone, the most popular elastic–plastic or thermo-mechanical method (TMM) considers temperature-dependent isotropic hardening rule and heat source model. For verification purpose, experimental analysis was conducted as bead-on-plate process with austenitic stainless steel material SS316L using GMAW robotic welding. It can be concluded that TMM can predict the total experimental angular strain with mean percentage error up to ca. 7% compared to ISM with 19% for weld kinematics and 29% for user defined. In terms of computational time, ISM gave higher potential to be implemented with only 10% of TMM.

**Keywords** FEM · Bead-on-plate · SS316L · TMM · ISM

## 1 Introduction

Welding is commonly used for assembling various parts of goods in the automotive, marine, aviation, and other industrial sectors. Despite of many advantages, deformation caused by welding processes such as gas metal arc welding (GMAW) is a typical and inevitable problem in fabrication industries. The rapid heating and cooling process leads to incompatible thermal strains, non-uniform expansion, and contraction of the weld zone in which the surrounding will cause permanent deformation of component. Distortion or strain induced by welding has an adverse impact not only on the dimensional accuracy of manufacturing, the assembly of structures and parts, efficiency, and productivity, but also on fatigue life reduction which can make a significant rise in cost of production and repair. An effective method of analysis to estimate welding deformation in industrial manufacturing is therefore essential which should be commenced before the actual welding process.

It is well known that effective and precise predictions of deformation and residual stress are crucial for structural integrity of welded structures. Theoretically or experimentally, numerous researchers have given attempts in approximating the thermal–mechanical behaviour of the welding. Numerical approach studies using FEM can upsurge existing knowledge to reduce production cost and lead time by providing virtual trial-and-error approach prior to products fabrication [1]. A recommendation by Ueda and Yamakawa et al. was proposed using FEM to simulate the

✉ Yupiter H. P. Manurung
yupiter.manurung@uitm.edu.my

[1] Smart Manufacturing Research Institute (SMRI) and College of Engineering, Universiti Teknologi MARA (UiTM), Shah Alam, Malaysia

[2] Jabatan Kejuruteraan Mekanikal, Politeknik Sultan Salahuddin Abdul Aziz Shah, Shah Alam, Malaysia

[3] Institute of Structural Durability and Railway Technology, Graz University of Technology, Graz, Austria

[4] NDT Lab and Metrology Lab, Nusantara Technologies Sdn. Bhd., Shah Alam, Malaysia

Published online: 03 February 2022



Content courtesy of Springer Nature, terms of use apply. Rights reserved.

thermo elastic–plastic phenomenon during welding [2]. The employment of heat source combination between conical and double ellipsoid was investigated in estimating deformation induced by the electron beam welding [3].

Since 1970, FEM has been progressively implemented in predicting and controlling welding deformation [4]. Numerical computation study on welded structure distortion can be performed in large and complex parts. However, it is costly in terms of fabrication capital and time. In recent years, inherent strain theory has been adopted with many implementations of large-scale and complex components, especially ship-buildings, offshore, and maritime structures [5, 6]. Thus, the ISM is highly recommended because of the inexpensive and straightforward technique that applies only elastic numerical modelling to analyse the stresses and weld distortions of large-scale parts.

The evolution of plastic and thermal strain induced by welding generates the formation of stress and welding distortion or strain. Thus, inherent strain is referred to as a basis of residual stress and welding deformation. Inherent strains are always present in the weld materials and its adjacent region, where the structures are subjected to high thermal gradients due to heat input. Deng et al. employed numerical calculation using thermal elastic–plastic numerical method and ISM to simulate the deformation of huge welded-structures with an experimental study as a verification purpose [7]. A fundamental study on modified inherent strain theory was conducted to calculate the residual deformation of large part-scale components generated by the direct metal laser sintering (DMLS) process [8].

Based on past literatures, there were only few attempts in comparative investigation on welding deformation or strain prediction with different numerical approaches, namely, the commonly-used ISM-user defined, novel ISM-weld kinematics, and the well-known thermo-mechanical method (TMM). Hence, the primary objectives of this research are to find the accuracy of numerical methods compared to experiment and to observe the computational time. In order to replicate the actual experiment, this research was conducted by considering the thermal calibration in finding suitable heat transfer coefficient, the plasticity model of evolved material after welding, the hardness value, and the simplified meshing strategy with sensitivity analysis. The cooling curve of thermal profile on the substrate between the simulated data and experiment was calibrated by adjusting the heat transfer coefficient. Further, the initial inherent strain value was calculated empirically regarding process parameters, physical properties, and as effective area where the inherent strain shall be distributed based on defined weld or hardness distribution. It is expected that the accuracy and computational time can be obtained and discussed as the basis for future additive manufacturing research. Moreover, this investigation can become the basis for the implementation in the metal additive manufacturing with larger scale, especially using direct energy deposition such as wire arc additive manufacturing or laser deposition method.

## 2 Modelling and numerical computation for welding distortion analysis

Welding distortions or strains at the initial phase of product design of process development can be fully understood using practical tools of numerical computation analysis based on the FE method. Hence, this ensures that adjustments to the process design can be performed to correct welding effects before the manufacturing process begins. Furthermore, this numerical procedure for predicting the mechanical behaviour of the welding process would save a significant amount of time and in-house production cost compared to the approach of post-welding distortion correction and mechanical properties improvement. However, the mechanical behaviour affects the actual structural engineering industry and it is a tremendously challenging task to predict the welding distortion due to the material phase transformation during the heating, melting and solidification process, and the complexity of the welding process during manufacturing. While methods for simulating the multi-disciplinary physics of welding are still extensively researched, thermo-mechanical elastic–plastic FEM for solid bodies is beneficial for welding simulations. Therefore, a complete 3D numerical simulation analysis of bead-on-plate was performed by utilizing numerical tool MSC Marc/Mentat in analysing the welding process of SS316L.

### 2.1 Geometrical and material modelling

Figure 1 illustrates that structural geometrical bead-on-plate modelling was created with 5799 nodes and 3560 solid elements. The element type was designed to be hexahedral solid structural full integration. An efficient FE model comprises three geometries namely weld bead, substrate, and welding table. The geometrical dimension for the substrate is designed as 140 mm ($l$) × 60 mm ($w$) × 4 mm ($t$). Each solid body element was segmented with hexagonal shape meshing type. As a result, the mesh in the weld materials and its neighbouring area, namely, HAZ, became finer, more consistent, and uniform. A simplified rectangular geometry shape was developed to model the weld bead with a thickness of 4 mm as to avoid extensive pre-processing and decrease calculation time during the post-processing stage.

Figure 2 demonstrates the assigned structural boundary condition by applying structural clamping load on the substrate in negative $Y$-axis. The specified structural clamping load positions on the substrate are designed similar with the actual application of the experiment.



Content courtesy of Springer Nature, terms of use apply. Rights reserved.

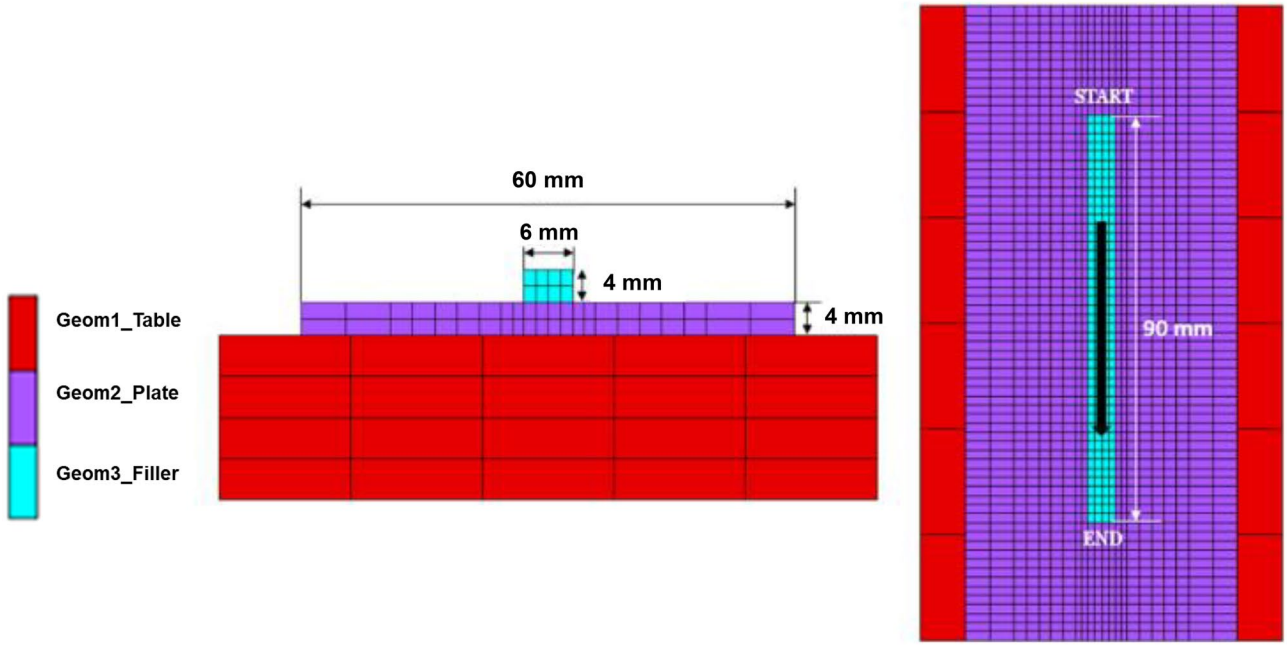



**Fig. 1** The geometrical modelling of bead-on-plate

The non-uniform temperature fields cause structure deformation with thermal stresses, which affect the thermal mechanical-physical material properties. Since material of SS316L was applied as a substrate and weld filler, phase transformation was assumed negligible and hence insignificant in this FEM simulation. The thermal expansion coefficient, thermal conductivity, specific heat capacity, and Young's modulus of SS316L are shown in Fig. 3 as non-linear material properties depending on temperature.

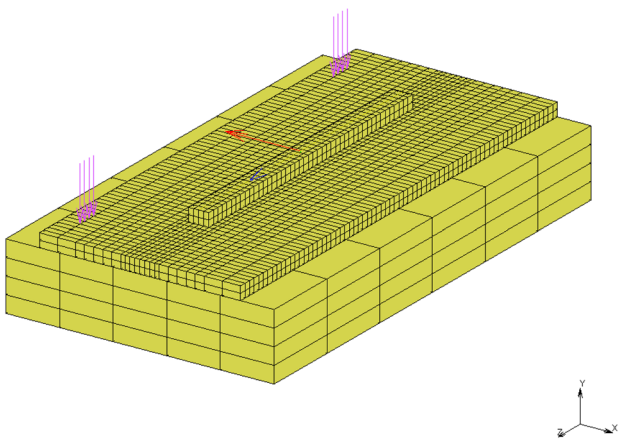


**Fig. 2** The modelling of structural clamping positions of bead-on-plate

Apart from mechanical and physical properties as shown in Fig. 3, analysis using TMM requires plasticity model to compute residual stress and distortion or strain induced by welding. For TMM, flow stresses were modelled using the isotropic hardening rule and Von Mises yield criterion to define the plastic behaviour. Figure 4 depicts the connection between flow stress and true plastic strain of SS316L at strain rates of 0.001 $s^{-1}$.

## 2.2 Numerical computational methods

Recent developments with mathematical modelling and numerical computation of welding phenomena provide researchers with powerful tools to broadly investigate the thermo-mechanical behaviour. Numerical computation analysis is executed utilising the FE method, which increases the cost for large-welded structures by considering the highly nonlinear thermo-mechanical welding behaviour. Despite the enormous computational costs, an efficient and straightforward linear finite-element method of simplification should be employed. In the meantime, an efficient approach of ISM is performed to investigate welding deformation where the plastic strain arises during welding processes. This study executes nonlinear TMM numerical analysis and elastic ISM for bead-on-plate model to analyse the angular strain of SS316L induced by GMAW.



Content courtesy of Springer Nature, terms of use apply. Rights reserved.

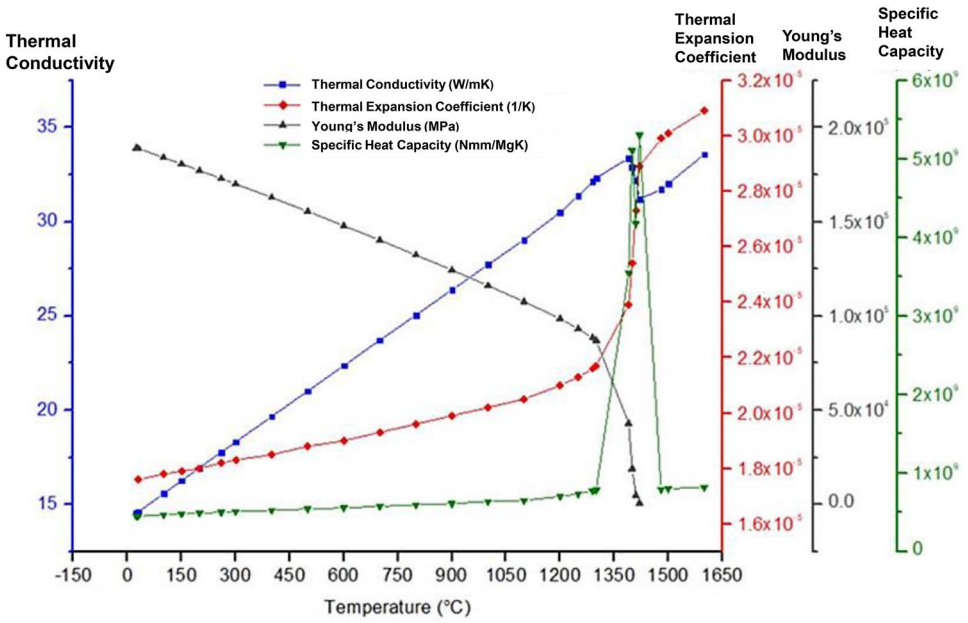



**Fig. 3** Temperature-dependent mechanical and physical properties of SS316L

### 2.2.1 Welding distortion analysis using TMM

Due to the fact that welding process can be seen as coupled tasks, the thermomechanical method commonly solves the welding problems in a consecutive manner. In the first stage of simulation, the transient thermal analysis is carried out and nodal temperature histories are imported into the subsequent mechanical analysis. Therefore, it is possible to model transient distortions and residual stresses. This model describes the moving welding torch by using a time increment technique which can produce similar predictions to the actual welding process. The coupled thermomechanical method assumes that thermal behaviour influences mechanical behaviour. However, the mechanical response does not influence the thermal analysis. A flow diagram of the thermo-mechanical simulation of the welding process is shown in Fig. 5. At time $t_i$, the thermal problem is solved initially, followed by the application of thermal loading to the mechanical problem. At time $t_{i+1}$, the deposit geometry is changed by adding material attributes. After each stable thermal iteration scheme, the material properties are updated. The prior computed data at $t_i$ is applied to initiate the thermal and mechanical problems. This updated material is employed as an input to the mechanical iteration method, which calculates stresses, strains, and deformations. Over time $t_{i+1}$, these two calculations are restarted. Due to the large temperature gradient generated, the thermal problem is solved using an enthalpy formulation to accelerate numerical convergence and consider the latent heat of fusion.

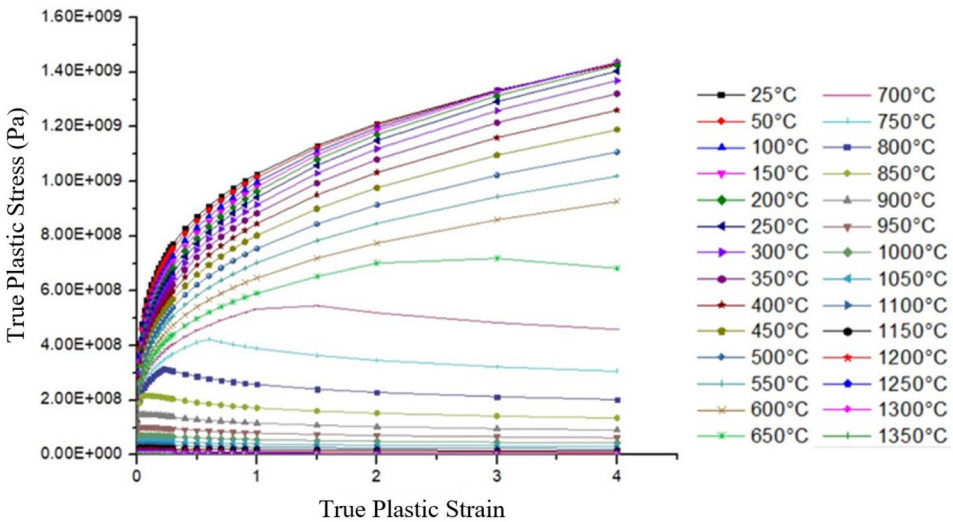



**Fig. 4** Flow curves of SS316L material at strain rate of 0.001 $s^{-1}$



Content courtesy of Springer Nature, terms of use apply. Rights reserved.

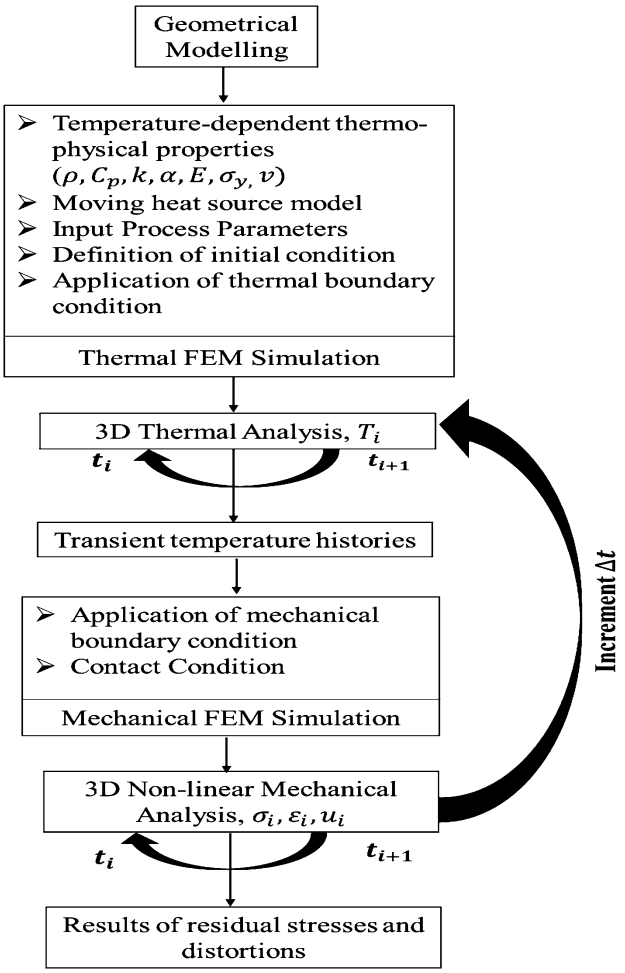



**Fig. 5** The coupled thermo-mechanical analysis

The thermal analysis is conducted using the thermal equilibrium solution of transient energy balance. The governing differential equation for transient thermal analysis of welding process can be defined as

$$\rho c \frac{\partial T}{\partial t}(x, y, z, t) = -\nabla . q(x, y, z, t) + Q(x, y, z, t) \tag{1}$$

where $\rho$, $c$, $T$, $q$, and $Q$ are the density of the materials (g/mm$^3$), specific heat capacity (J g$^{-1}$ °C$^{-1}$), current temperature (°C), heat flux (W/mm$^2$), and heat input per unit volume (W/mm$^3$), respectively. Meanwhile, $x$, $y$, and $z$ are the coordinates in the reference system (mm), $t$ is the time (s), and $\nabla$ is the spatial gradient operator. The distribution of heat through the body part using the temperature gradients is characterized by Fourier's heat flux conduction equation, where $k$ is the isotropic temperature dependent thermal conductivity (J/(mms °C)):

$$q_{\text{cond}} = -k \nabla T \tag{2}$$

During welding process, total heat losses may occur through convection, thermal radiation, or conduction by fixturing body parts. Newton's law of cooling defines heat loss due to convection ($q_{\text{conv}}$) as follows:

$$q_{\text{conv}} = h_{\text{conv}}(T_s - T_0) \tag{3}$$

where $h_{\text{conv}}$, $T_s$, and $T_0$ are the heat transfer coefficient, surface temperature of the weldment, and ambient temperature, respectively. Meanwhile, the Stefan-Boltzmann law expresses the heat flux due to radiation as

$$q_{\text{rad}} = \varepsilon \sigma (T_s^4 - T_0^4) \tag{4}$$

where $\varepsilon$ and $\sigma$ are the surface emissivity and Stefan–Boltzmann constant ($\sigma = 5.67 \times 10 - 8$ W/m$^2$ K$^4$), respectively. In this study, the ambient temperature is assumed to be 30 °C.

Double ellipsoid heat source model by Goldak et al. is ideal for describing the density of heat power generated by an electric arc travelling across a flat surface plate. The heat flux with power density distribution in Goldak's double ellipsoid comprises front quadrant ($Q_{vf}$) and rear quadrant ($Q_{vr}$) throughout the welding path and trajectory which can be generated using Eq. (5) [9].

$$Q_{vf/r}(x, y, z) = \frac{6\sqrt{3} f_{f/r} Q}{abc_{f/r}\pi\sqrt{\pi}} e^{-3\frac{x^2}{a^2}} . e^{-3\frac{y^2}{b^2}} . e^{-3\frac{z^2}{c_{f/r}^2}} \tag{5}$$

The fractions of deposition heads $f_f$ and $f_r$ describe the heat distribution of the heat flux in the front and rear quadrants, assuming that the condition $f_f + f_r = 2$ is fulfilled. If the volumetric heat source is defined as the power density equation of the moving heat source and the value of each direction utilised in the GMAW simulation, the fractions can be considered to be $f_f = \frac{2a_f}{a_f + a_r}$ and $f_r = \frac{2a_f}{a_f + a_r}$.

Heat source modelling is one of the difficult tasks in the computational simulation of the arc welding process. Heat source models such as the Goldak's double ellipsoid model are commonly employed as heat sources in arc welding simulations. This is because it accurately and consistently represents the pattern and distribution of heat flux. This numerical computation analysis employs Goldak's double ellipsoid model as the volumetric heat source to imitate the actual distribution of heat distribution using the GMAW process in the filler material. Figure 6 depicts the common heat source model of Goldak's double ellipsoid with a Gaussian distribution.

In Goldak's double ellipsoid model, the direction of heat flux distribution is defined by the dimensions of width ($a$), depth ($b$), rear length ($c_r$), and front length ($c_f$). Therefore, the numerical computation procedure in this study was based on previous research works conducted by the authors with few modifications and improvements in a way



Content courtesy of Springer Nature, terms of use apply. Rights reserved.

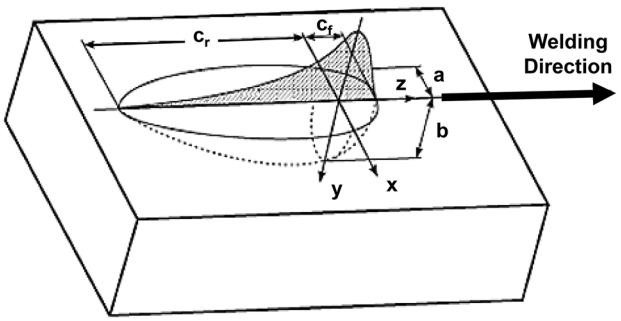



**Fig. 6** Heat source modelling of Goldak's double ellipsoid [10]

to attain better results [11]. Table 1 displays the details of each direction applied in the thermal volume weld flux boundary conditions.

Table 2 lists the simulation parameters designated for the TMM-based analysis of the bead-on-plate model. For the accurate FEM simulation, the consideration of arc efficiency, $\eta$, for the GMAW is crucial and assumed to be 0.8 [12]. The element birth approach was utilized to simulate the filler material. Initially, all weld material elements were deactivated beforehand the beginning of the numerical analysis, and then, the elements were activated in a sequential manner following the application of the heat source.

The mechanical analysis is performed using the thermal analysis or temperature field as input. The elastic strain–stress relationship is modelled using the isotropic strain hardening rule, whereas the plastic behaviour is evaluated using the Von Misses criteria [13]. The mechanical analysis can be modelled by deriving the total strain increment from the equation as follows:

$$\Delta\varepsilon = \Delta\varepsilon^{\text{elastic}} + \Delta\varepsilon^{\text{plastic}} + \Delta\varepsilon^{\text{thermal}} + \Delta\varepsilon^{\text{creep}} + \Delta\varepsilon^{\text{phase}} \tag{6}$$

where $\Delta\varepsilon^{\text{elastic}}$, $\Delta\varepsilon^{\text{plastic}}$, $\Delta\varepsilon^{\text{thermal}}$, and $\Delta\varepsilon^{\text{creep}}$ are denoted as elastic, plastic, thermal, and creep strain increments, respectively. The strain generated by the phase transformation is denoted by $\Delta\varepsilon^{\text{phase}}$. However, the phase-transformation associated strain increment was ignored in the present study since it had a negligible contribution to the total strain in austenitic stainless steel SS316L. $\Delta\varepsilon^{\text{phase}}$ was also not taken into account in this investigation since the bead-on-plate of GMAW process experienced a very short heating process.

**Table 1** Heat source parameters of Goldak's double ellipsoid

| Heat source dimensions | Value |
|---|---|
| Width ($a$) | 5 mm |
| Depth ($b$) | 5.5 mm |
| Front Length ($c_f$) | 4 mm |
| Rear Length ($c_r$) | 10 mm |

**Table 2** Welding simulation parameters

| Current ($I$) | Voltage ($V$) | Travel speed ($v$) |
|---|---|---|
| **172 A** | 20 V | 6 mm/s |

Three parameters characterize the plasticity model, namely, the yield criterion, the flow rule, and the hardening law [14, 15]. The von Mises yield criterion given by Eq. (8) is the most extensively used model for plasticity, where $\sigma_1, \sigma_2$, and $\sigma_3$ are the major stresses. Some researchers have used von Mises' yield criterion in their investigations to estimate residual stresses and welding deformation [16–19]. According to the flow rule, the plastic flow is orthogonal to the yield surface.

$$\sigma_y = \sqrt{\frac{(\sigma_1 - \sigma_2)^2 + (\sigma_2 - \sigma_3)^2 + (\sigma_3 - \sigma_1)^2}{2}} \tag{7}$$

A hardening law governs the calculation on the amount of plastic flow and the evolution of yield strength of the material [20]. The isotropic hardening law is applied to simulate a bead-on-plate model without taking phase transformation into account. Equation (8) represents the relationship between stress and strain of the assigned material:

$$\sigma = \sigma_y + H(\varepsilon^p)^N \tag{8}$$

where $\sigma$, $\sigma_y$, $H$, $\varepsilon^p$, and $N$ denote total stress, initial yield stress, hardening law coefficient, plastic strain, and hardening law exponent, respectively.

### 2.2.2 Welding distortion analysis using ISM

Structural welding component is typically categorized into three parts, namely, the weld region, the heat affected zone, and the base metal region [21]. The inherent strain zone refers to the weld region and its nearby area, which experience a locally high temperature gradient. When welding is completed, plastic strains are also developed. Both the weld zone and HAZ experience higher thermal cycles above the critical temperature which then cool to ambient temperature when the welding process is completed. The remaining plastic strains are considered the inherent strains. Therefore, the base metal zone is also recognized as the elastic region because its material properties remain elastic at ambient temperature. The final stresses are given by Eq. (9),

$$\Delta\varepsilon^{\text{total}} = \Delta\varepsilon^{\text{elastic}} + \Delta\varepsilon^{\text{plastic}} + \Delta\varepsilon^{\text{thermal}} + \Delta\varepsilon^{\text{creep}} \tag{9}$$

The creep strain becomes smaller and negligible throughout the cooling process [5]. In austenitic stainless steel, phase transformation does not affect welding deformation



Content courtesy of Springer Nature, terms of use apply. Rights reserved.

[22, 23]. Thermal strain is also reduced to zero. As a result, the total strain sum can be expressed in Eq. (10) as

$$\Delta\varepsilon^{\text{total}} = \Delta\varepsilon^{\text{elastic}} + \Delta\varepsilon^{\text{plastic}} \tag{10}$$

Furthermore, Eq. (10) can be rearranged to become Eq. (11);

$$\Delta\varepsilon^{\text{plastic}} = \Delta\varepsilon^{\text{total}} - \Delta\varepsilon^{\text{elastic}} \tag{11}$$

Next, at the end of the cooling phase, the inherent strain equals the plastic strain, as displayed in Eq. (12) [24, 25].

$$\Delta\varepsilon^{*} = \Delta\varepsilon^{\text{total}} - \Delta\varepsilon^{\text{elastic}} = \Delta\varepsilon^{\text{plastic}} \tag{12}$$

Due to the maximum temperatures within the weld region, inherent strains behave differently. Therefore, the compressive plastic strains with plastic strain region in the welding zone and its surrounding areas at the end of each thermal cycle remain constant as the total of inherent strain in the welding phase [26, 27].

The maximum temperature causes residual plastic strains during the welding process, resulting in inherent strains within the weld region and the heat affected zone. A direct and simplified method based on elastic FEM simulation to compute residual stress and welding distortion produced by T-joint and I-joint using inherent strain was proposed in [5]. The thermal load of units used is associated with the inherent strain value in the linear elastic FE model. The following equation is a definition of total inherent stress in the welding process:

$$\varepsilon = -W/A \tag{13}$$

If the longitudinal and transverse inherent strains including the area and the location where the strains occur are known in advance, the welding deformation can be simulated using the elastic analysis of ISM. The total amount of welding shrinkage per unit length is denoted by W. $A$ signifies the area in which the inherent strains are present. Since $W$ is the entire welding shrinkage created by the thermal load, the relationship between longitudinal shrinkage $W_x$, transverse shrinkage $W_y$, and heat input $Q$ is as follows.

$$W_x = KQ \tag{14}$$

$$W_y = \xi Q \tag{15}$$

Following Eq. (9), Eq. (10) summarizes $K$ and $\xi$, which consist of the thick coefficients and the range that can be defined as large thick to sheet metal using a simplified analytical approach [7]. As a calibration purpose, these two ranges of $K$ and $\xi$ coefficient values can be adjusted in order to predict the mechanical behaviour of welding simulation. In this equation, $\alpha$ is defined as the thermal expansion coefficient, $\rho$ is the mass density, and $C_p$ is referred as the specific heat capacity.

$$K = (0.255 - 0.335)\ \alpha/\ \rho C_p \tag{16}$$

$$\xi = (0.255 - 1.0)\ \alpha/\rho C_p \tag{17}$$

The total amount of the inherent strain can be determined using Eqs. (18) and (19) which are then loaded using the following formulae.

$$\varepsilon_x^* = \frac{W_x}{A} \tag{18}$$

$$\varepsilon_y^* = \frac{W_y}{A} \tag{19}$$

where $A$ is the element's effective area as a result of the inherent strain distribution. Therefore, the size and geometry of effective area can be calibrated using macrograph analysis or Hardness test. Another approach to compute residual plastic strains is by calculating the generated inherent strain at the highest temperature in the weld region and heat affected zone during the welding processes. The thermal expansion coefficient can be employed to express the different longitudinal and transverse compression on the weld region [28]. The following equation is applied to load the unit temperature into the node,

$$\varepsilon^* = \frac{W}{A} = \alpha\ \Delta T \tag{20}$$

The elastic inherent strain method was used in this analysis to compute the weld deformation by applying the inherent strain to the weld zone and its surrounding region. The ranges of $K$ and $\xi$ coefficient values were adjusted. In this study, Eqs. (16) and (17) were applied to compute the initial inherent strain value, while considering the welding process parameters and physical properties. Based on the mathematical framework analysis method presented in Fig. 7, the numerical calculation tool MSC Marc/Mentat can be utilized to forecast welding distortion and residual stress. However, the focus of this study is primarily on bead-on-plate substrate strain.

By performing an elastic FEM analysis, the welding deformation can be computed by imposing the inherent strain value in the structural boundary condition. Figure 8 shows $\{f\}$, $\{\varepsilon^*\}$, $\{u\}$, $\{\sigma\}$, and $\{\varepsilon^e\}$ are regarded as vectors of equivalent nodal force, inherent strain, nodal displacement, residual stress, and elastic strain, respectively. Meanwhile, $[B]$, $[D]$, and $[K]$ are differentiator matrix, constitutive matrix, and stiffness matrix, respectively. Based on general elastic FEM analysis, the welding displacement is computed by the applied structural load per unit stiffness.

In this research, numerical computation software MSC Marc/Mentat provides two different approaches to apply inherent strain as structural boundary conditions. The



Content courtesy of Springer Nature, terms of use apply. Rights reserved.

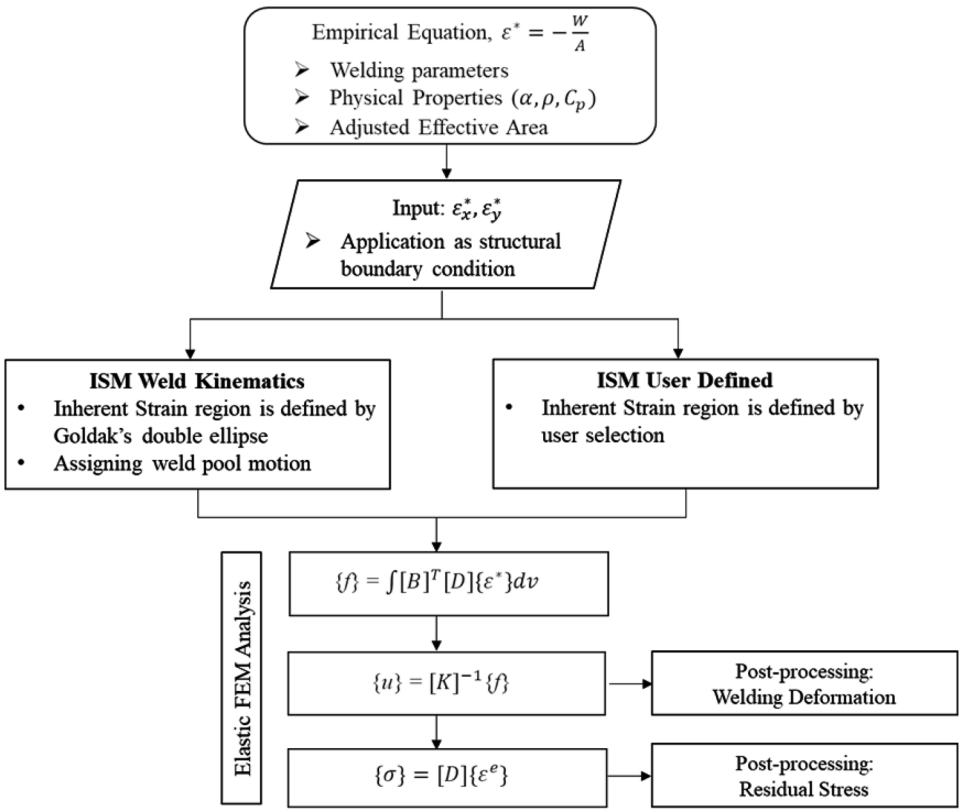



**Fig. 7** Mathematical framework of deformation or strain analysis procedure using ISM

approaches are known as user defined and weld kinematics. The application of inherent strain needs to define the heat affected zone (HAZ) which is the portion of assembly subjected to high temperature during welding process. By using user defined option, HAZ is defined by user selection where all the elements defined by the user are assigned as the inherent strain. Meanwhile, the HAZ is defined by applying weld kinematics option in which the inherent strains in this approach are assigned under consideration of integration points falling inside the moving weld pool. Furthermore, the weld pool dimension shall be considered similar with Goldak's double ellipsoid heat source model. The weld pool dimension applied in this simulation will be the same as the Goldak's heat source dimension used in thermo-mechanical FEM as shown in Table 4.

The coefficients $K$ and $\xi$ considered in the longitudinal inherent $\varepsilon_x^*$ and the transverse inherent strain $\varepsilon_y^*$ are adjusted to characterize the prediction of welding strain. The inherent strain distribution occurs along the fusion zone and the adjacent region of the substrate material. Figure 8 demonstrates the bead-on-plate model with isometric and front view demonstrating the effective areas of 44 $mm^2$ of the element that employed the inherent strain as the structural boundary conditions and the coefficients $K$ and $\xi$.

Equations (18) and (19) are used to compute the longitudinal and transverse inherent stresses, where the thermal expansion coefficient $\alpha$, specific heat capacity $C_p$, and mass density are $1.456\times10^{-5}$ $K^{-1}$, 0.45 $Jg^{-1}$ $K^{-1}$, and $7.966\times10^{-3}$ $gmm^{-3}$, respectively. The longitudinal inherent strain occurs primarily along the weld line, while the transverse inherent

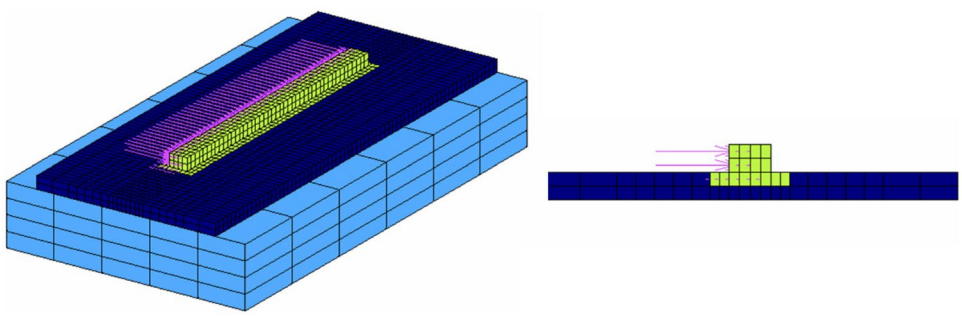


**Fig. 8** The selected elements for assigning inherent strain with consideration of effective area



Content courtesy of Springer Nature, terms of use apply. Rights reserved.

**Table 3** Calculated inherent strain value with adjusted $K$ and $\xi$

| Inherent strain | Value |
|---|---|
| Longitudinal inherent strain $\varepsilon_z^*$ | −0.01296 |
| Transverse inherent strain $\varepsilon_x^*$ | −0.015249 |

strain is denoted as the perpendicular weld lateral inherent strain. In this simulation, the longitudinal inherent strain is considered in the $z$-axis, whereby the transverse inherent strain is in the $x$-axis. The initial computed inherent strain used in the numerical computation, as well as the associated effective areas, is listed in Table 3.

### 2.3 Thermal calibration and mesh sensitivity analysis

The application of thermocouples in the actual experiment is designed to calibrate the numerical computation analysis, particularly for the adjusted heat transfer coefficients to the environment and other elements components. Table 4 presents the thermal boundary conditions employed within the FEM simulation.

The weld bead has glued contact with the substrate to measure heat transfer between the elements. The numerical parameters assigned within the model of SS316L latent heat have thermal properties of 256.4 kJ/kg in this TMM simulation of bead-on-plate. Meanwhile, the solidus and liquidus temperatures of SS316L are assigned as 1279 °C and 1450 °C, respectively. Figure 9 illustrates the measured and simulated temperature fields on the substrate of SS316L.

The number and size of finite element modelling meshes can have a significant effect on model behaviour, accuracy, and calculation time. Employing smaller meshes in the model under the same conditions should increase the accuracy of the numerical results. However, long computational time and a large amount of data storage space are acquired to perform and complete the job. Furthermore, to generate temperature distribution and stress fields with the fewest yet optimal number of elements in the model, a well-balanced meshing strategy should be utilized.

A mesh sensitivity analysis was conducted in order to determine the optimal size and number of meshes for the model. The investigation was carried out on five designed models by subdividing the elements with varying thickness and width. The geometry of the base plate employed in this work was identical to the one applied in the experiment. Due to the weld bead materials and the heat affected zone encounter high temperature gradients, more subdivision and smaller meshes size were applied in this area. The weld bead and heat affected zone element models were partitioned in the $x$-direction with widths of 6 mm, 3 mm, 2 mm, 1 mm, and 0.75 mm. Figure 10 depicts the coarser and finer element mesh models, denoted as Model 1 and Model 2, respectively.

**Table 4** Calibrated numerical boundary conditions on bead-on-plate of SS316L

| Numerical parameters | Value |
|---|---|
| Heat transfer coefficient (metal to Metal) | 2000 W/m$^2$/K |
| Heat transfer coefficient (metal to environment) (W/m$^2$/K) | 45 W/m$^2$/K |
| Initial temperature | 30 °C |

The sensitivity analysis was analysed based on the maximum temperature affected by the amounts of elements meshing. Figure 11 displays the maximum temperature for various number of elements of the bead-on-plate model. The maximum temperature almost equals to 370 ˚C when the number of elements exceeds 3000. Meanwhile, the peak temperature attained for models with fewer elements indicates approximately around a 16% inaccuracy percentage with experiments. The 3000-element model is appropriate for TMM and ISM numerical analysis.

## 3 Experimental set-up and procedure

The experimental set-up and procedure for this study consisted measurement of temperature fields using type-K thermocouple angular substrate strain of bead-on-plate which employed coordinate measurement machine (CMM) and calibration of effective area by Vickers hardness test. The investigation of bead-on-plate was executed using GMAW robotic welding system of ABB IRB 2400/16 equipped with KEMMPI Pro Evolution ProMIG 540MXE power source as shown in Fig. 12.

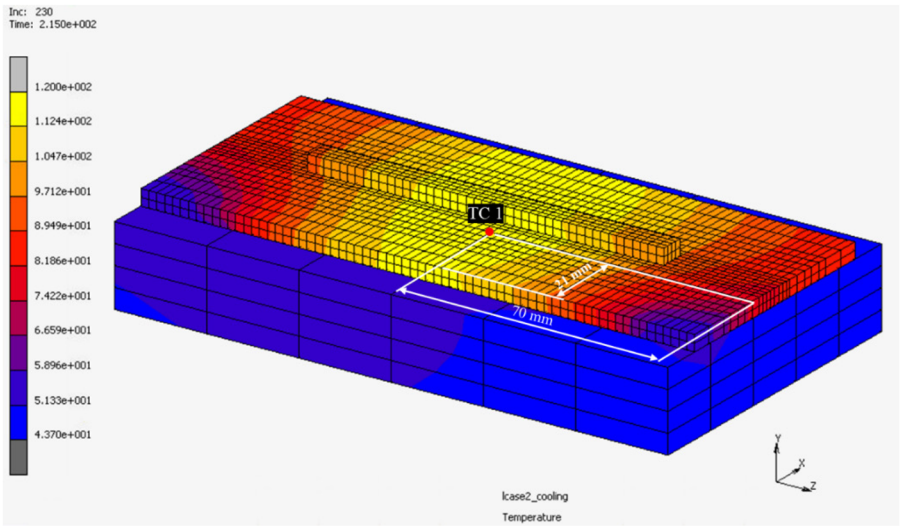
In this experimental work, a filler material of austenitic stainless steel ER316LSi with a diameter of 1.2 mm was deposited into the substrate material of SS316L. This standard designation filler material is particularly suitable for structural steel welding in accordance with AWS standard. Table 5 demonstrates the chemical composition of SS316L and ER316LSi provided by the manufacturer.

The tests were performed by setting the values of process parameters of GMAW welding process which included arc current ($I$), voltage ($V$), travel speed ($v$), and wire feed rate (wfr) as tabulated in Table 6.

As for temperature measurement, type-K thermocouple was integrated at corresponding positions in the substrate as shown in Fig. 13. The twisted reference junction of thermocouples was attached on the substrate to a thin sheet metal by using Kyowa GW-3C spot welder. Therefore, the thermocouples were placed in the middle of the substrate with an approximate length of 70 mm. To calibrate the thermal cycles of simulated bead-on-plate, real measured temperature history was recorded by using data logger



Content courtesy of Springer Nature, terms of use apply. Rights reserved.



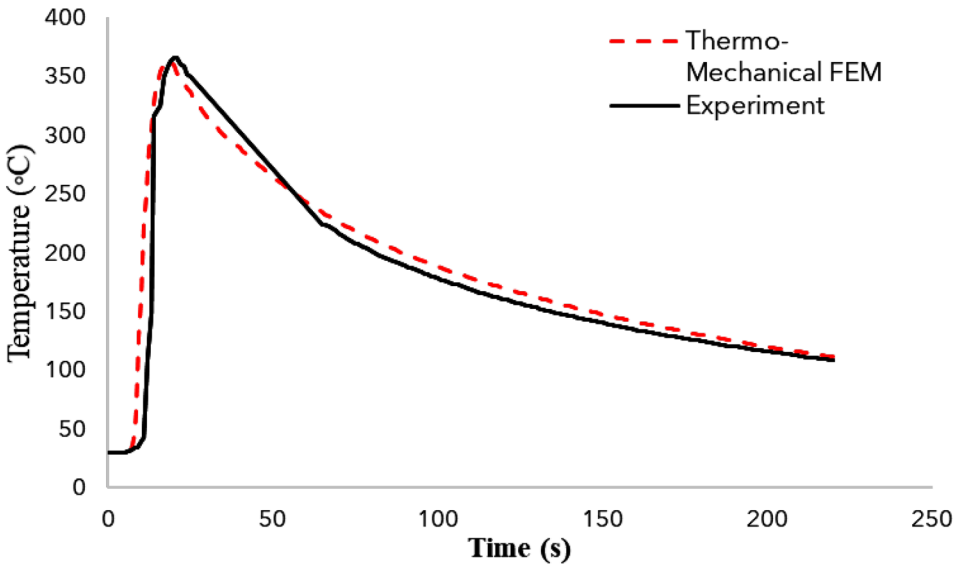




**Fig. 9** Schematic thermocouple position (top) and comparison of measured and simulated transient temperature distribution of bead-on-plate of SS316L (bottom)

ALMEMO 2890-9d. As a result, the temperature fields of bead-on-plate were calibrated with the FEM model to define the adjusted major heat transfer coefficients.

As verification technique of substrate strain measurement, coordinate measuring machine (CMM) as shown in Fig. 14 was required to determine the pre-condition of substrate strain

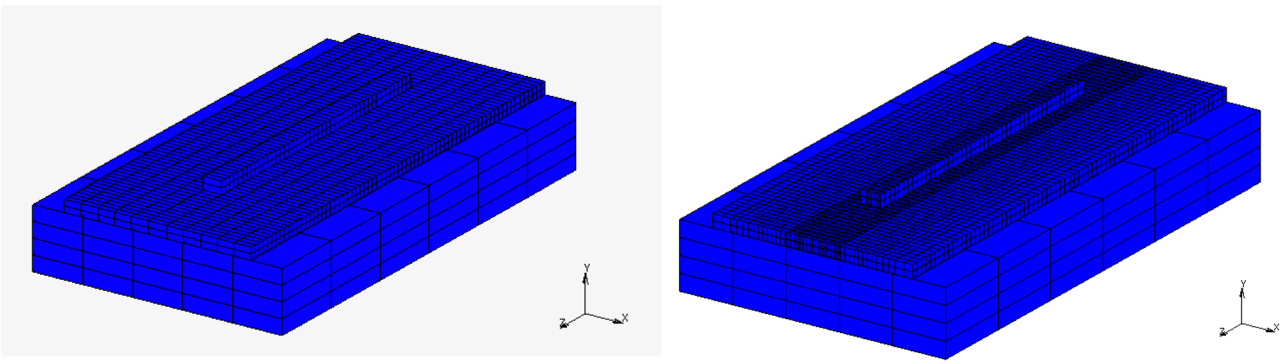


**Fig. 10** A constant of element mesh model with the width of 6 mm (left) and the elements with 0.75 mm near welded line and 3 mm on edge (right)



Content courtesy of Springer Nature, terms of use apply. Rights reserved.

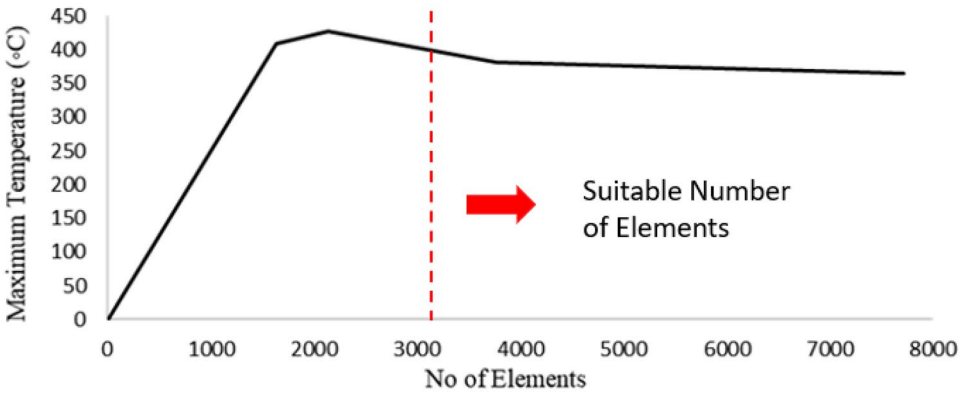



**Fig. 11** Sensitivity analysis on maximum temperature

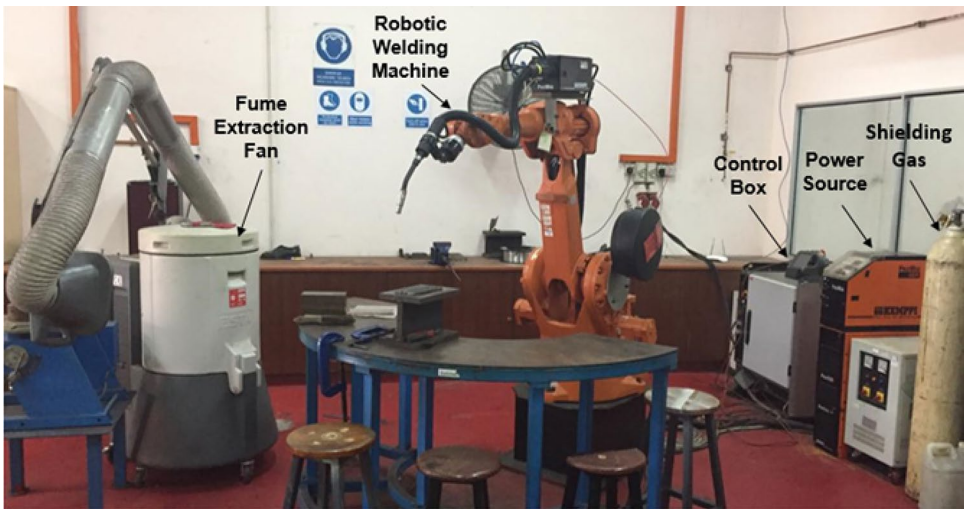



**Fig. 12** ABB IRB 2400/16 Robotic welding system equipped with KEMMPI ProMig 540 MXE power source

**Table 5** Chemical compositions of SS316L and ER316LSi

| Material | C | Cu | Cr | Mn | Mo | Ni | S | Si | P |
|---|---|---|---|---|---|---|---|---|---|
| **SS316L** | 0.03 | 0.19 | 18.0 | 2.0 | 3.0 | 14.0 | 0.03 | 0.002 | 0.045 |
| **ER316LSi** | 0.02 | - | 19 | 1.4 | 12.5 | 2.6 | 0.02 | 0.85 | 0.025 |

prior to the experimental work and post-condition strain after the accomplishment of bead-on-plate of GMAW process.

Further, a chemical composition analysis of the welded component was performed using a SEM/EDX microscope. The SEM-EDX Hi-Tech Instrument SU3500 was used to analyse the material composition of an Oerlikon Inertfil 316LSi welded component. Figure 15 depicts the specimen

**Table 6** The parameters of GMAW process

| Parameters | Value |
|---|---|
| **Current (*A*)** | 162–172 |
| **Voltage (*V*)** | 16–20 |
| **Travel speed (mm/s)** | 6 |
| **Wire feed rate (m/min)** | 6 |
| **Shielding gas** | 100% argon |

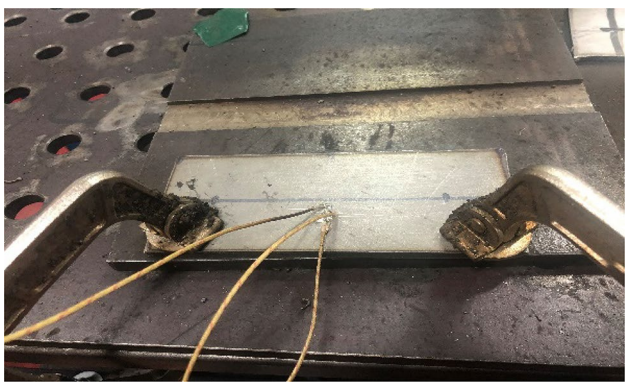


**Fig. 13** Thermocouple positions on the substrate



Content courtesy of Springer Nature, terms of use apply. Rights reserved.

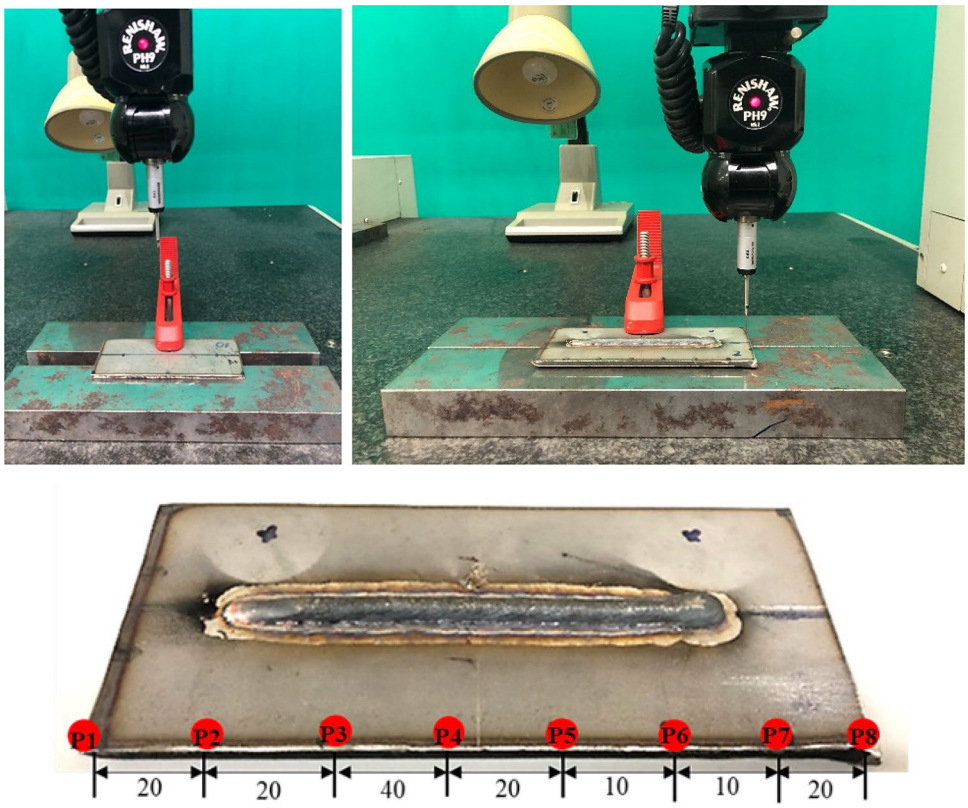



**Fig. 14** Pre and post measurement of angular substrate strain is conducted using CMM

sample and SEM/EDX results. Meanwhile, Table 7 shows the chemical composition of evolved filler material of SS316L. Hence, a material modelling of SS316L was generated using advanced material tool JMATPRO based on the chemical composition result.

Effective area is subjected to the highest temperature during welding process. Hence, it is one of the crucial components in the estimation of initial inherent strain. Since the inherent strain happens along the weld region and heat affected zone of the weld specimen, Vickers hardness test is performed to define the geometrical size and region of weld zone and HAZ.

In this study, the Vickers hardness measurement was conducted on the etched specimen of bead-on-plate of SS316L with a load of 1 kgf. The aim was to distinguish the exact region of welding parts that comprised of the weld metal, HAZ, and base metal. Besides, the HAZ geometry was essential to estimate the effective area of inherent strain value. The hardness values were measured and plotted in Fig. 16. The hardness profile was taken at 1.85 mm and 2.75 mm from the bottom line of the substrate. Figure 16 illustrates the variation of the hardness of the bead-on-plate specimen at different zone such as weld zone, HAZ, and base metal. As shown by hardness

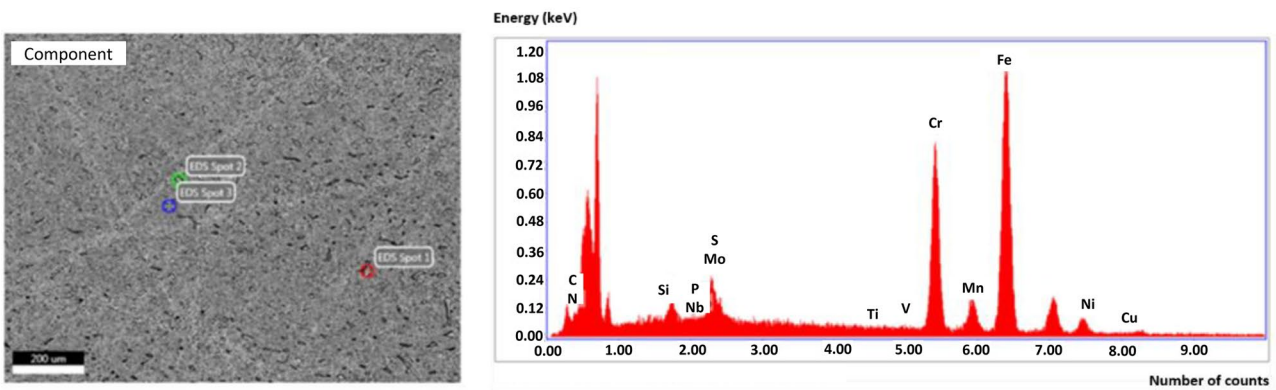



**Fig. 15** Results of chemical composition using SEM–EDX on bead



Content courtesy of Springer Nature, terms of use apply. Rights reserved.

**Table 7** Chemical composition of evolved filler material of SS316L

| Material | C | Cu | Cr | Mn | Mo | N | Ni | S | Si | Ti | V | P |
|---|---|---|---|---|---|---|---|---|---|---|---|---|
| Component | 0.03 | 0.76 | 17.83 | 2.43 | 1.63 | - | 10.57 | - | 0.63 | 0.267 | 0.3 | - |

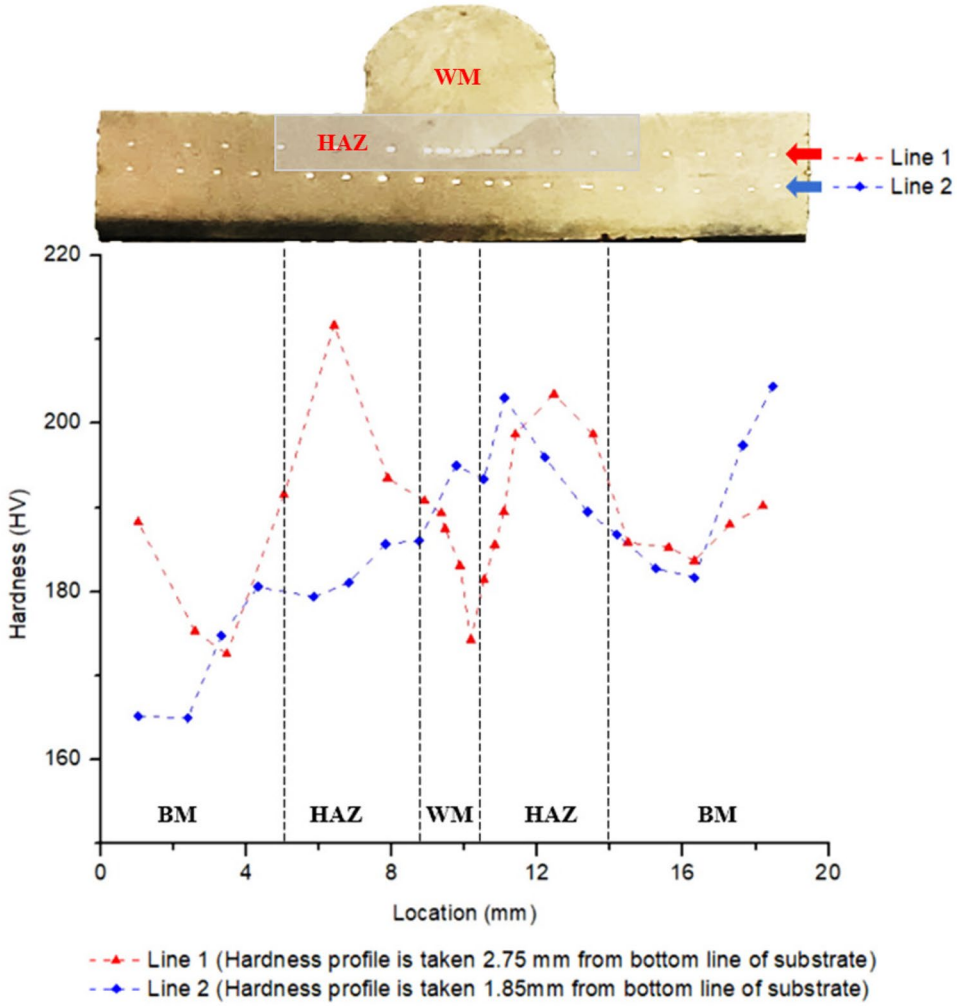



**Fig. 16** Vickers hardness values induced by GMAW of bead-on-plate of SS316L

profile of Line 1 in Fig. 13, the hardness value of the HAZ was greater than weld zone and base metal. The hardness value of HAZ was between 190 and 215 HV which was within the range of the past research [29]. The higher value in the hardness of HAZ may be attributed to the finer grains of the HAZ as compared to the weld zone and base metal [30]. Meanwhile, the hardness reduced as the location measurement moved to Line 2 in which this area was expected to be heat unaffected zone.

The determination of effective area is essential for computing the initial longitudinal and transverse inherent strain value by using empirical formula as stated in Eqs. (18) and (19] respectively. Hence, it is also essential to select and assign the respective element of FEM model where the inherent strain will be loaded as the boundary conditions. For a better and correct numerical analysis of inherent strain method, the effective area was measured based on the measurement of weld zone and HAZ geometry under hardness test as shown in Fig. 17.

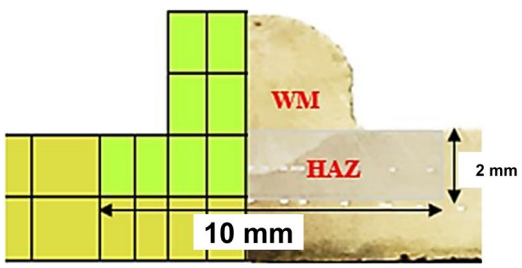



**Fig. 17** Calibration of effective area of weld zone and HAZ of bead-on-plate



Content courtesy of Springer Nature, terms of use apply. Rights reserved.

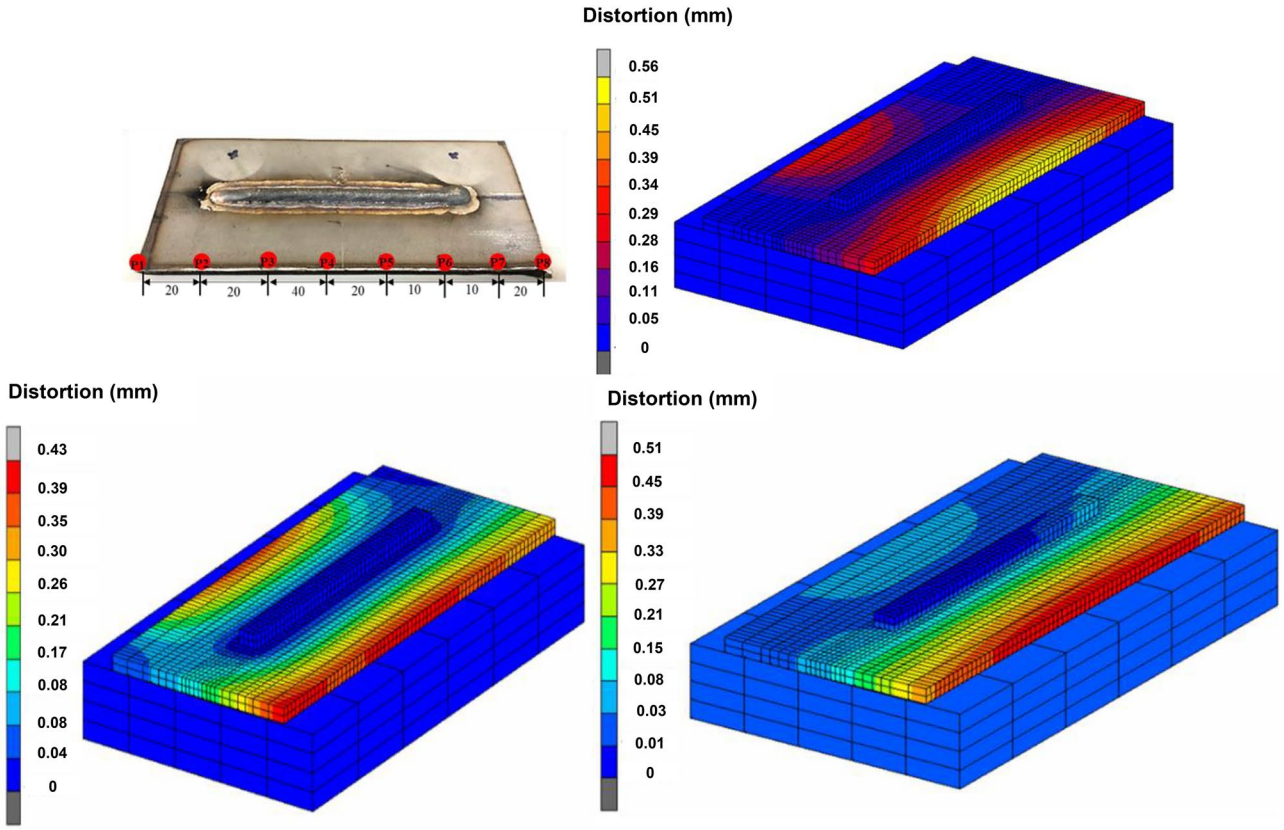



**Fig. 18** Comparison of substrate strain: thermo-mechanical method (top-right), ISM-user defined (bottom-left), and ISM weld kinematics (bottom-right)

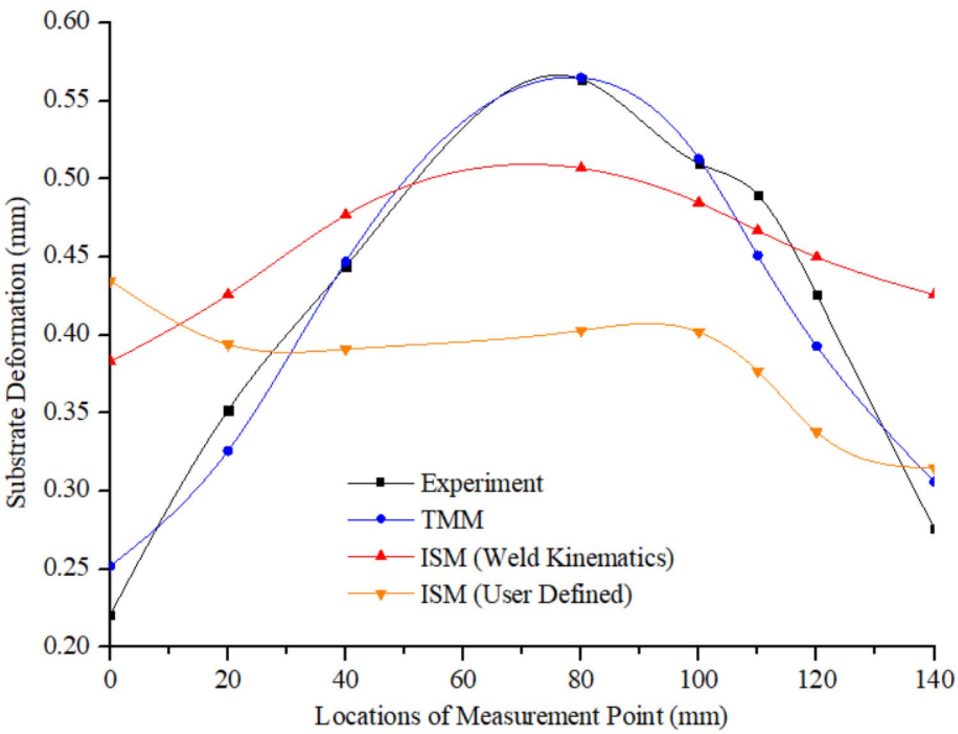



**Fig. 19** Results of substrate strain between experiment, TMM, and ISMs



Content courtesy of Springer Nature, terms of use apply. Rights reserved.

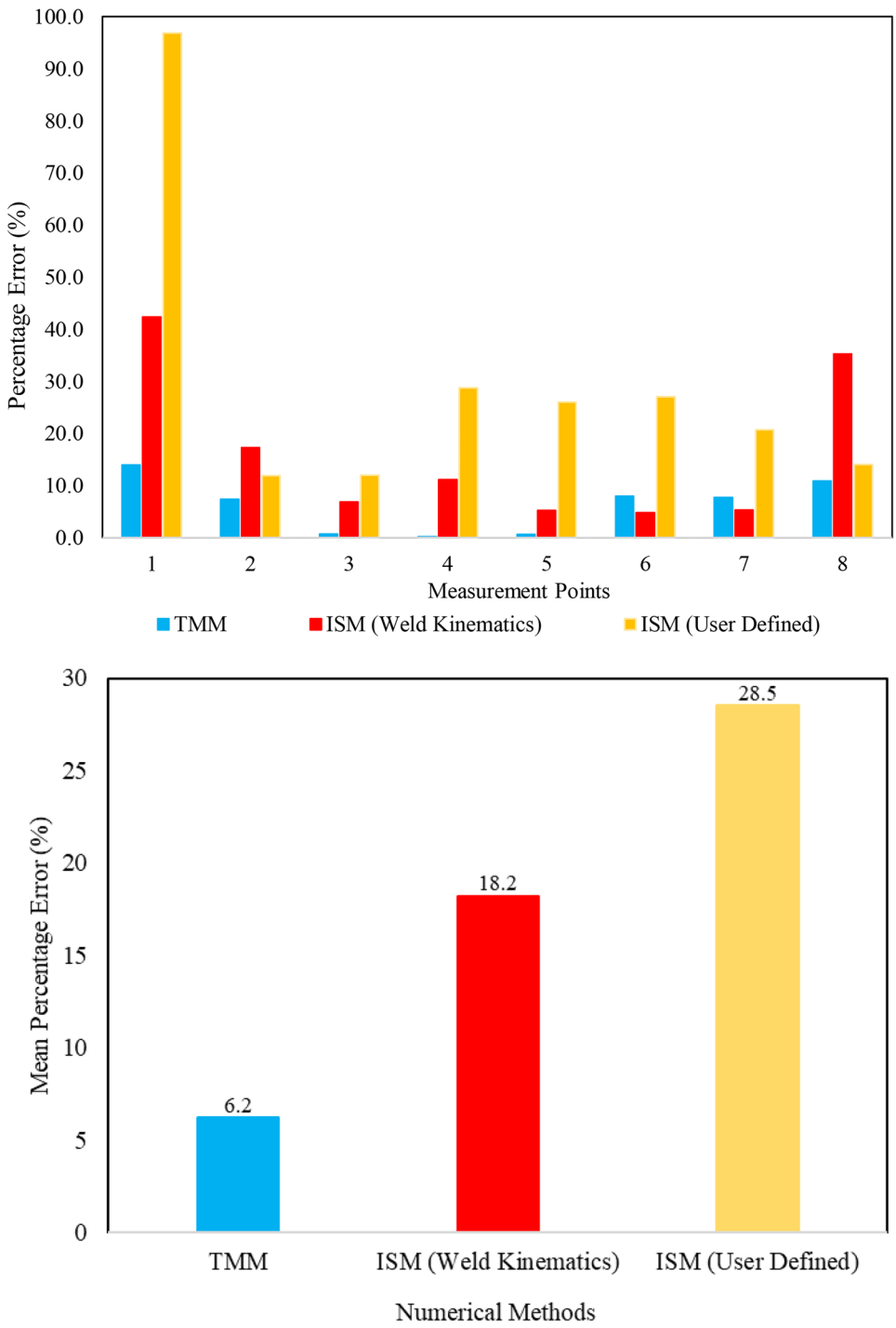



**Fig. 20** Comparison of percentage error on the substrate angular strain at particular measurement points: relative (top) and mean (bottom)

## 4 Results and discussions

Figure 18 displays a schematic of eight CMM measurement locations along the edge of the plate, as well as an analysis of the contour band of substrate strain generated by the GMAW process using the ISM and TMM numerical computation analysis. The contour band display can be utilised to analyse the correlation between inherent strain and final substrate strain using the FE model. It shows that the inherent strain approach computes the maximum substrate strain at the side edge corresponding to the clamping constraint condition.

This signifies that the proposed ISM can be used to forecast the welding angular strain if the inherent strain is known beforehand. The largest inherent strain region occurs in the weld filler and its surrounding area, or HAZ, where the most



Content courtesy of Springer Nature, terms of use apply. Rights reserved.

localized transient heat input has been generated. Figure 19 compares the simulated results of bead-on-plate using all three FEM approaches and experiment on substrate strain.

Figure 20 shows the relative percentage error of substrate strain between TMM simulated data of FEM simulation and ISM. The inherent strain method using weld kinematics and user defined features demonstrates promising and potential method in predicting substrate strain of either complex or simple structural geometrical components. In comparison, the weld kinematics of inherent strain method provides greater precision than the user defined. This is due to the application of ISM using weld kinematics option using the definition of Goldak's double ellipse definition of heat source for the inherent strain distribution.

In TMM-based numerical simulation, the most important parameters are material modelling and heat transfer coefficient beside geometry and other constraints. In case experimental analysis of material, material modelling use advanced software. While the rely on database value might result in insufficient result, heat transfer coefficients can be obtained and adjusted by using experimental temperature measurement using thermocouple. To examine the effect of the ISM parameters on the substrate angular strain of the bead-on-plate model, numerical simulations are carried out under consideration of adjusted coefficient values of $K$, $\xi$, and effective areas using approaches provided in MSC Marc/Mentat.

According to the findings, the highest strain occurs in the middle of the substrate edge at the unclamped area which corresponds to constraint conditions. The discrepancy in average error of strain values appears to be in the range up to 28.5% between numerical methods and experimental results which can be caused due to the fluctuating WAAM process parameters and complex nonlinearity of thermomechanical material properties. This percentage error result is comparable to the investigation conducted in [31] which showed the value up to 25% between experiment and simulation. With regard to location of maximum strain, the investigation in [32] showed similar tendency at the middle of plate edge.

Based on the Figs. 18 and 19, it can also be seen than the maximum strains symmetrically in the middle section of the edges without clamping. Although the strains on the other side of the plate were not measured numerically, the simulation result can be adequate since the numerical error is within the acceptable range as a result of several experimental attempts.

The TMM simulation takes longer to compute due to complexity of welding behaviour and nonlinear temperature-dependent material properties. Figure 21 depicts the computational time of the TMM and ISM numerical analysis for bead-on-plate model. It indicates that the elastic inherent strain method of FEM simulation to compute welding strain analysis improves the computational time. As a result, the ISM can save up to 90% of calculation time which can be also observed similarly from investigation conducted in [33]. Hence, this finding shows that numerical procedure based on ISM has the potential to analyse the mechanical behaviour of large-scale structure within shorter time with acceptable accuracy.

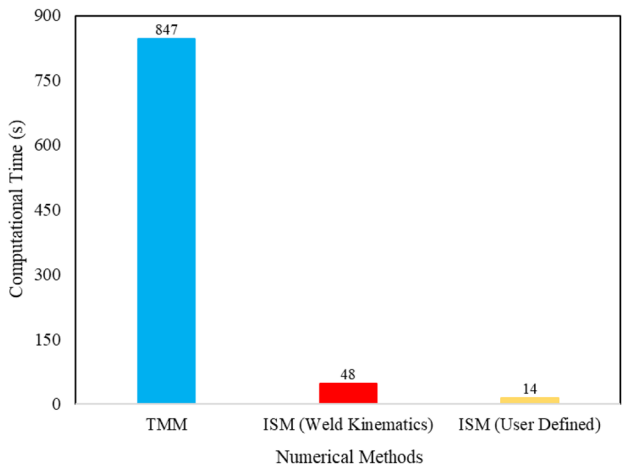



**Fig. 21** Comparison of CPU-time

## 5 Conclusion

The bead-on-plate of SS316L can be modelled by employing numerical tool MSC Marc/Mentat in predicting the weld induced strains on the substrate by adopting elastic ISM and TMM-based FEM analysis. Bead-on-plate simulations were carried out using the same geometrical modelling, which included a simplified rectangular shape and meshing of the weld bead in both cases. The longitudinal inherent strain $\varepsilon_z^*$ and transverse inherent strain $\varepsilon_x^*$, derived from the proposed inherent strain theory, were used to compute the angular welding strain using elastic FEM simulation, whereby TMM-based simulation considered the nonlinear material model and adjusted heat transfer coefficients. A comparison was made between the results obtained by experiment and those three numerical simulation methods. According on the outcomes of this study, the following conclusions can be drawn:

1. The numerical computation on angular substrate strain analysis of bead-on-plate model was successfully performed by implementing nonlinear TMM and elastic ISM under the consideration of process parameters, physical properties, and effective area.
2. By using TMM, heat transfer coefficients were adjusted based on transient thermal distribution which might differ to commonly used database value.
3. By using ISM, coefficient values of $K$ and $\xi$ were adjusted to predict substrate angular strain. It is essen-



Content courtesy of Springer Nature, terms of use apply. Rights reserved.

tial to determine the effective areas where the inherent strains are distributed based on the inherent strain theory. The inherent longitudinal and transverse strains were applied on the weld bead and heat effected zone.
4. Sensitivity analysis is of importance to find the optimized mesh size or number in order to obtain proper results.
5. In terms of accuracy, TMM still offers the best result with 6.18%, followed by ISM Weld Kinematics with 18.23% and ISM-user defined with 28.53% if compared to experimental investigation.
6. In terms of computational time, ISM speeds up with only ca. 10% of TMM.

For further recommendation, extensive research can be executed utilizing inherent strain method on more layers a.k.a. WAAM and other materials.

**Acknowledgements** The authors would like to express their gratitude to the staff members of Smart Manufacturing Research Institute (SMRI) and Research Interest Group: Advanced Manufacturing Technology (RIG:AMT) at School of Mechanical Engineering, Universiti Teknologi MARA (UiTM) Shah Alam for encouraging this research.

**Author contribution** Siti Nursyahirah Ahmad: Writing manuscript, simulation of TMM and ISM. Yupiter HP Manurung: Experiment using Robotic Welding and Simulation of TMM. Keval P Prajadhiana: Experiment using Robotic Welding. Yusuf O. Busari: Writing manuscript. Muhd Faiz Mat: Writing manuscript and measurement using CMM. NorAsiah Muhammad: Writing manuscript and measurement using CMM. Martin Leitner: Writing manuscript and analysis. Salina Saidin: Writing manuscript and analysis.

**Funding** This research is financially supported by ASEA-UNINET grant with the project number ASEA 2019/Montan/1, ERASMUS + (Montan University in Leoben), Geran Penyelidikan Khas (GPK) with Project Code: 600-RMC/GPK 5/3 (123/2020), Geran Konsortium Kecemerlangan Penyelidikan (Large Volume Additive Manufacturing/LVAM) from Ministry of Higher Education (MOHE) in Malaysia, Geran Penyelidikan Khas (GPK) with Project Code: 600-RMC/GPK 5/3 (123/2020), and Technogerma Engineering and Consulting Sdn. Bhd. with Project Code: TEC/SMRI/2020–2021/01.

## Declarations

**Ethical approval** This article does not contain any studies with human participants or animals performed by any of the authors.

**Consent to participate** Not applicable.

**Consent for publication** Not applicable.

**Conflict of interest** The authors declare no competing interests.

## References

1. Ueda Y, Yamakawa T (1971) Analysis of thermal elastic-plastic stress and strain during welding by finite element method. Trans Japan Weld Soc 2(2):90–100
2. Liang W, Deng D, Sone S, Murakawa H (2005) Prediction of welding distortion by elastic finite element analysis using inherent deformation estimated through inverse analysis. Weld World 49:30–39. https://doi.org/10.1007/BF03266500
3. Lundbäck A (2003) Finite element modelling and simulation of welding of aerospace components, Luleå University of Technology
4. Ueda Y, Yamakawa T (1973) Analysis of thermal elastic-plastic behavior of metals during welding by finite element method. J Japan Weld Soc 42(6):567–577. https://doi.org/10.2207/qjjws1943.42.567
5. Luo Y, Murakawa H, Ueda Y (1996) Prediction of welding deformation and residual stress by elastic fem based on inherent strain (Report I): Mechanism of inherent strain production(mechanics, strength & structure design). Trans JWRI 26:49–57
6. Birk-Sørensen M (1999) Simulation of welding distortions in ship section, Technical University of Denmark
7. Deng D, Murakawa H, Liang W (2007) Numerical simulation of welding distortion in large structures. Comput Methods Appl Mech Eng 196(45–48):4613–4627. https://doi.org/10.1016/j.cma.2007.05.023
8. Liang X, Cheng L, Chen Q, Yang Q, To AC (2018) A modified method for estimating inherent strains from detailed process simulation for fast residual distortion prediction of single-walled structures fabricated by directed energy deposition. Addit Manuf 23:471–486. https://doi.org/10.1016/j.addma.2018.08.029
9. Malik AM, Qureshi EM, Ullah Dar N, Khan I (2008) Analysis of circumferentially arc welded thin-walled cylinders to investigate the residual stress fields. Thin-Walled Struct 46(12):1391–1401. https://doi.org/10.1016/j.tws.2008.03.011
10. Goldak JA, Akhlaghi M (2005) Computational welding mechanics. Springer International Publishing, US. https://doi.org/10.1007/b101137
11. Ahmad SN, Manurung YHP, Taufek T, Leitner M (2021) Numerical simulation on residual stress and substrate deformation of bead-on-plate of ss316l using inherent strain method. Lect Notes Mech Eng 46:723–738. https://doi.org/10.1007/978-981-15-9505-9_65
12. Goldak J, Chakravarti A, Bibby M (1984) A new finite element model for welding heat sources. Metall Trans B 15(2):299–305. https://doi.org/10.1007/BF02667333
13. Zain-ul-abdein M, Nélias D, Jullien JF, Deloison D (2010) Experimental investigation and finite element simulation of laser beam welding induced residual stresses and distortions in thin sheets of AA 6056–T4. Mater Sci Eng A 527(12):3025–3039. https://doi.org/10.1016/j.msea.2010.01.054
14. Lindgren LE (2001) Finite element modeling and simulation of welding. Part 2: Improved material modeling. J Therm Stress 24(3):195–231. https://doi.org/10.1080/014957301300006380
15. Theofilos-Ioannis M (2012) Elastoplastic constitutive models in finite element analysis, National Technical University Athens
16. Asserin O, Loredo A, Petelet M, Iooss B (2011) Global sensitivity analysis in welding simulations — what are the material data you really need. Finite Elem Anal Des 47(9):1004–1016. https://doi.org/10.1016/j.finel.2011.03.016
17. Qureshi EM, Malik AM, Dar NU (2009) Residual stress fields due to varying tack welds orientation in circumferentially welded thin-walled cylinders. Adv Mech Eng 2009(10):1–9. https://doi.org/10.1155/2009/351369
18. Pasternak H, Launert B, Krausche T (2015) Welding of girders with thick plates — fabrication, measurement and simulation. J Constr Steel Res 115:407–416. https://doi.org/10.1016/j.jcsr.2015.08.037
19. Wang Q, Liu XS, Wang P, Xiong X, Fang HY (2017) Numerical simulation of residual stress in 10Ni5CrMoV steel weldments. J Mater Process Technol 240:77–86. https://doi.org/10.1016/j.jmatprotec.2016.09.011



Content courtesy of Springer Nature, terms of use apply. Rights reserved.

20. Ding J, Colegrove P, Mehnen J, Williams S, Wang F, Almeida PS (2014) A computationally efficient finite element model of wire and arc additive manufacturing. Int J Adv Manuf Technol 70:227–236. https://doi.org/10.1007/s00170-013-5261-x
21. Il Seo S, Jang CD (1999) Study on the prediction of deformations of welded ship structures. J Ship Prod 15(02):73–81. https://doi.org/10.5957/jsp.1999.15.2.73
22. Gouge M, Michaleris P (2017) Thermo-mechanical modeling of additive manufacturing. Elsevier Inc, First edit
23. Olson DL (1985) Prediction of austenitic weld metal microstructure and properties. Weld J (Miami, United States) 64(10). https://www.osti.gov/biblio/6129873. Accessed 17 Aug 2021
24. Kim TJ, Jang BS, Kang SW (2015) Welding deformation analysis based on improved equivalent strain method considering the effect of temperature gradients. Int J Nav Archit Ocean Eng 7(1):157–173. https://doi.org/10.1515/ijnaoe-2015-0012
25. Wang YX, Zhang P, Hou ZG, Li CZ (2008) Inherent strain method and thermal elastic-plastic analysis of welding deformation of a thin-wall beam. J Mech 24(4):301–309. https://doi.org/10.1017/S1727719100002434
26. Ueda Y, Murakawa H, Ma N (2013) Simulation procedures for welding heat conduction, welding deformation, and residual stresses using the FEM programs provided on the companion website. Elsevier, Welding Deformation and Residual Stress Prevention, pp 169–207
27. Jun-Mei C, Hao LU, Jian-Hua W et al (2002) Prediction of welding deformation with inherent strain method based on FEM. ANSYS Support
28. Jang CD, Lee CH, Ko DE (2002) Prediction of welding deformations of stiffened panels. Proc Inst Mech Eng Part M J Eng Marit Environ 216(2):133–143. https://doi.org/10.1243/147509002762224342
29. Moslemi N, Redzuan N, Ahmad N, Hor TN (2015) Effect of current on characteristic for 316 stainless steel welded joint including microstructure and mechanical properties. Proc CIRP 26:560–564. https://doi.org/10.1016/j.procir.2015.01.010
30. Joseph B, Katherasan D, Sathiya P et al (2012) Weld metal characterization of 316L(N) austenitic stainless steel by electron beam welding process. Int J Eng Sci Technol 4(2):69–176. https://doi.org/10.4314/ijest.v4i2.13
31. Ma N, Nakacho K, Ohta T, Ogawa N (2016) Inherent strain method for residual stress measurement and welding distortion prediction. ASME 2016 35th International Conference on Ocean, Offshore and Arctic Engineering. https://doi.org/10.1115/omae2016-54184
32. Venkatkumar D, Ravindran D (2019) Effect of boundary conditions on residual stresses and distortion in 316 stainless steel butt welded plate. High Temp Mater Proc 38:827–836. https://doi.org/10.1515/htmp-2019-0048
33. Zhu J, Khurshid M, Barsoum Z (2019) Accuracy of computational welding mechanics methods for estimation of angular distortion and residual stresses. Weld World 63:1391–1405. https://doi.org/10.1007/s40194-019-00746-9


**Publisher's Note** Springer Nature remains neutral with regard to jurisdictional claims in published maps and institutional affiliations.



Content courtesy of Springer Nature, terms of use apply. Rights reserved.

# Terms and Conditions

Springer Nature journal content, brought to you courtesy of Springer Nature Customer Service Center GmbH (“Springer Nature”).
Springer Nature supports a reasonable amount of sharing of research papers by authors, subscribers and authorised users (“Users”), for small-scale personal, non-commercial use provided that all copyright, trade and service marks and other proprietary notices are maintained. By accessing, sharing, receiving or otherwise using the Springer Nature journal content you agree to these terms of use (“Terms”). For these purposes, Springer Nature considers academic use (by researchers and students) to be non-commercial.
These Terms are supplementary and will apply in addition to any applicable website terms and conditions, a relevant site licence or a personal subscription. These Terms will prevail over any conflict or ambiguity with regards to the relevant terms, a site licence or a personal subscription (to the extent of the conflict or ambiguity only). For Creative Commons-licensed articles, the terms of the Creative Commons license used will apply.
We collect and use personal data to provide access to the Springer Nature journal content. We may also use these personal data internally within ResearchGate and Springer Nature and as agreed share it, in an anonymised way, for purposes of tracking, analysis and reporting. We will not otherwise disclose your personal data outside the ResearchGate or the Springer Nature group of companies unless we have your permission as detailed in the Privacy Policy.
While Users may use the Springer Nature journal content for small scale, personal non-commercial use, it is important to note that Users may not:

1. use such content for the purpose of providing other users with access on a regular or large scale basis or as a means to circumvent access control;
2. use such content where to do so would be considered a criminal or statutory offence in any jurisdiction, or gives rise to civil liability, or is otherwise unlawful;
3. falsely or misleadingly imply or suggest endorsement, approval , sponsorship, or association unless explicitly agreed to by Springer Nature in writing;
4. use bots or other automated methods to access the content or redirect messages
5. override any security feature or exclusionary protocol; or
6. share the content in order to create substitute for Springer Nature products or services or a systematic database of Springer Nature journal content.

In line with the restriction against commercial use, Springer Nature does not permit the creation of a product or service that creates revenue, royalties, rent or income from our content or its inclusion as part of a paid for service or for other commercial gain. Springer Nature journal content cannot be used for inter-library loans and librarians may not upload Springer Nature journal content on a large scale into their, or any other, institutional repository.
These terms of use are reviewed regularly and may be amended at any time. Springer Nature is not obligated to publish any information or content on this website and may remove it or features or functionality at our sole discretion, at any time with or without notice. Springer Nature may revoke this licence to you at any time and remove access to any copies of the Springer Nature journal content which have been saved.
To the fullest extent permitted by law, Springer Nature makes no warranties, representations or guarantees to Users, either express or implied with respect to the Springer nature journal content and all parties disclaim and waive any implied warranties or warranties imposed by law, including merchantability or fitness for any particular purpose.
Please note that these rights do not automatically extend to content, data or other material published by Springer Nature that may be licensed from third parties.
If you would like to use or distribute our Springer Nature journal content to a wider audience or on a regular basis or in any other manner not expressly permitted by these Terms, please contact Springer Nature at

onlineservice@springernature.com